Supplementary Information

A Spheres-in-Tube Carbonaceous Nanostructure for High-Capacity and High-Rate Lithium-Sulfur Batteries

Yuanhang Ge,[a]† Ze Chen,[a]† Sunjie Ye,[c] Zhifeng Zhu,[a] Yingfeng Tu,[a] and Xiaoming Yang*[ab]

[a] State and Local Joint Engineering Laboratory for Novel Functional Polymeric Materials, Suzhou Key Laboratory of Macromolecular Design and Precision Synthesis, Jiangsu Key Laboratory of Advanced Functional Polymer Design and Application, Department of Polymer Science and Engineering College of Chemistry, Chemical Engineering and Materials Science, Soochow University, Suzhou 215123, P. R. China.

[b] Key Laboratory of Advanced Textile Materials and Manufacturing Technology, Ministry of Education.

[c] School of Physics and Astronomy, University of Leeds, LS2, 9JT, Leeds, UK

†The two authors contribute equally to this work.

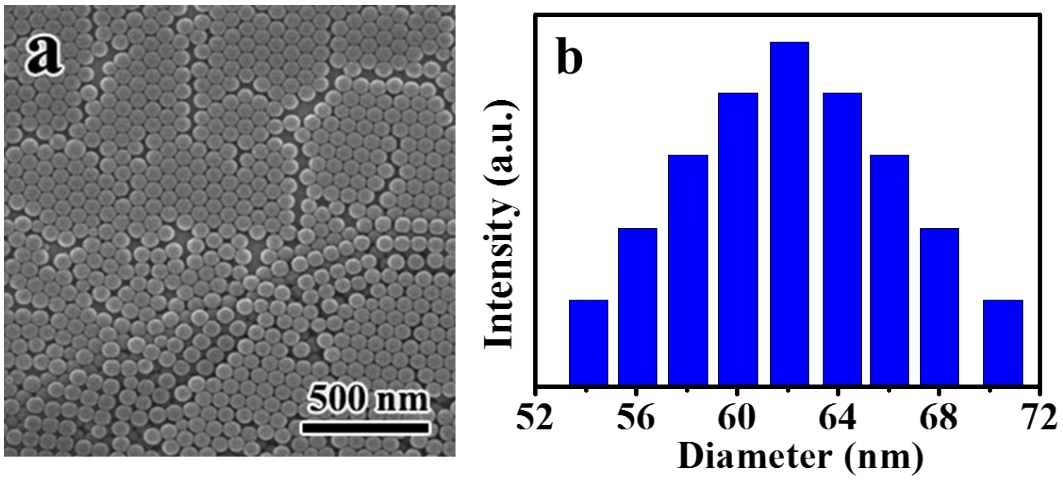

Fig. S1. SEM image and corresponding Dynamic Light Scattering result of SiO_2 nanoparticles prepared by traditional Stöber-Fink-Bohn method.

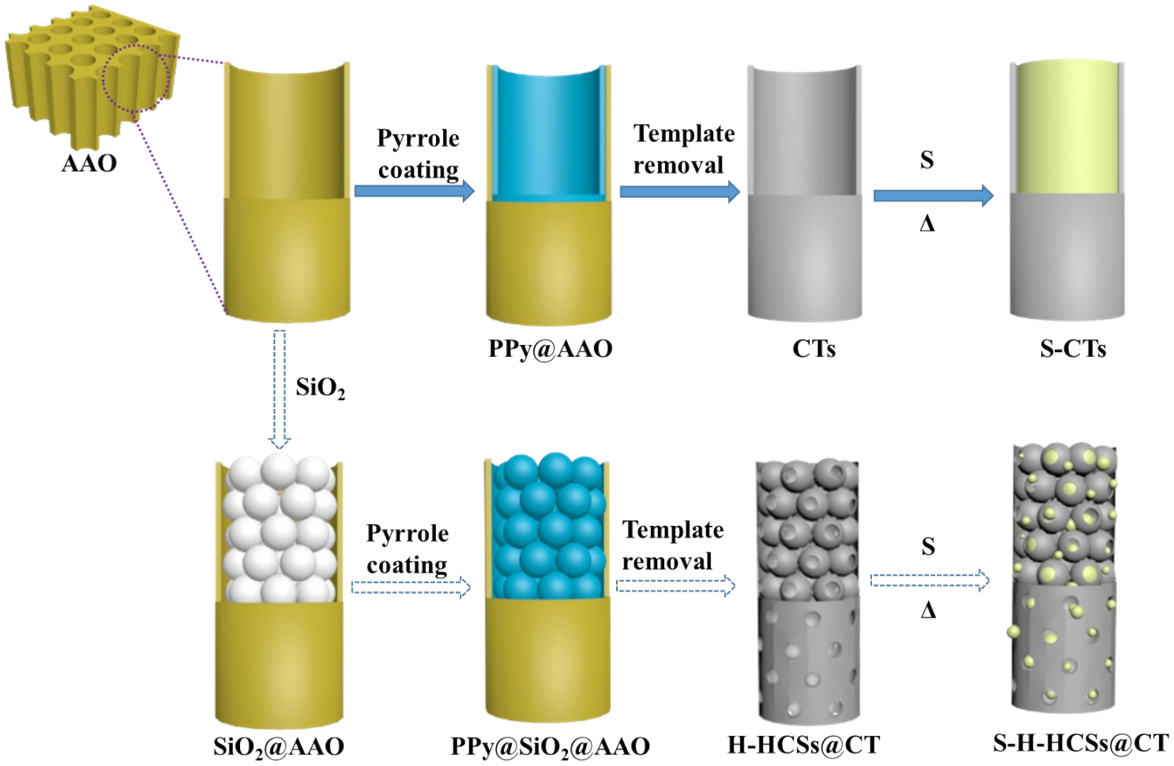

Fig. S2. Schematic illustration of the production of S-CTs and S-H-HCSs@CT.

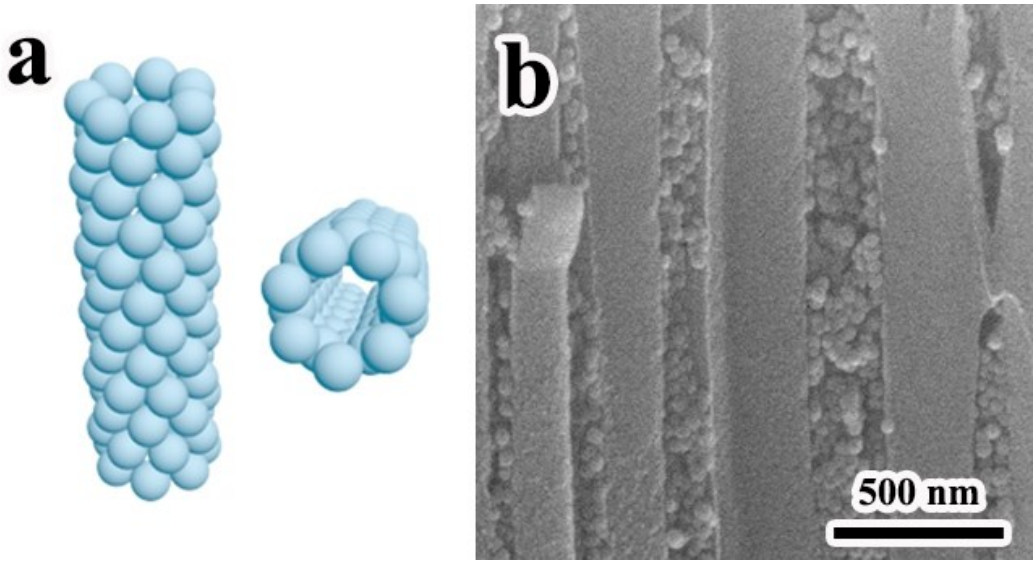

Fig. S3. Scheme models and related cross-sectional SEM images of confined assembled structure of SiO_2 in AAO a) α = 3.33 (α = *dc*/*ds*, *dc* means the AAO channel diameter, *ds* means the diameter of the SiO_2 NPs.)

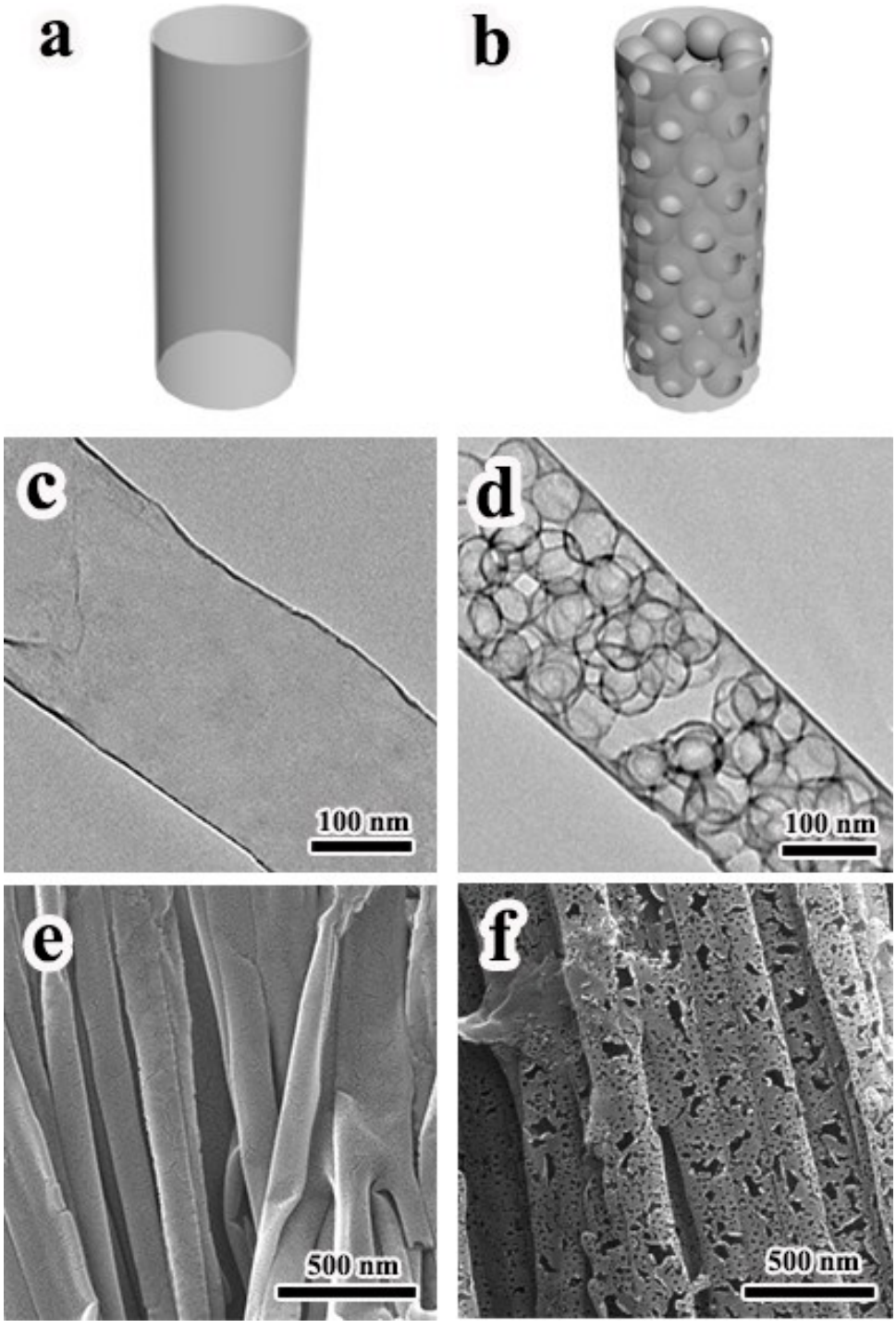

Fig. S4. Schematics of a) CTs and b) H-HCSs@CT. TEM and SEM images c) and e) show bare CTs. TEM and SEM images d) and f) show H-HCSs@CT with mesopores on the CT surface.

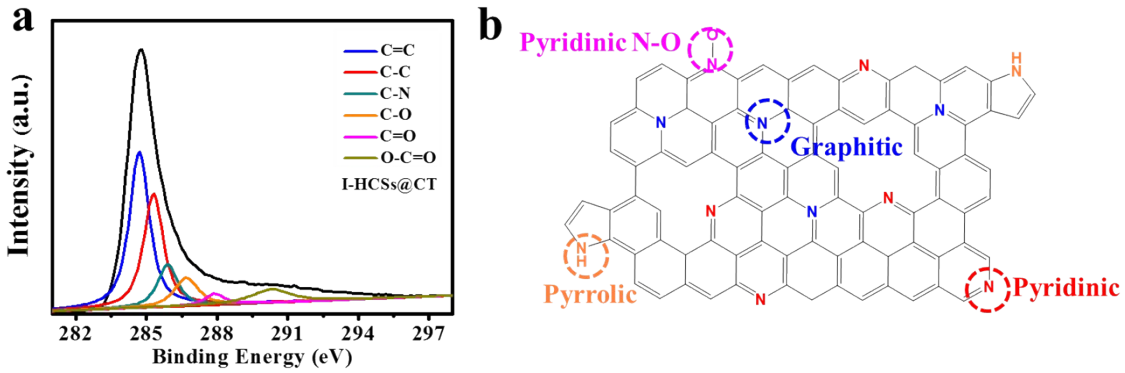

Fig. S5. a) High-resolution C1s XPS spectra of I-HCSs@CT; b) Schematic model of functional groups in I-HCSs@CT.

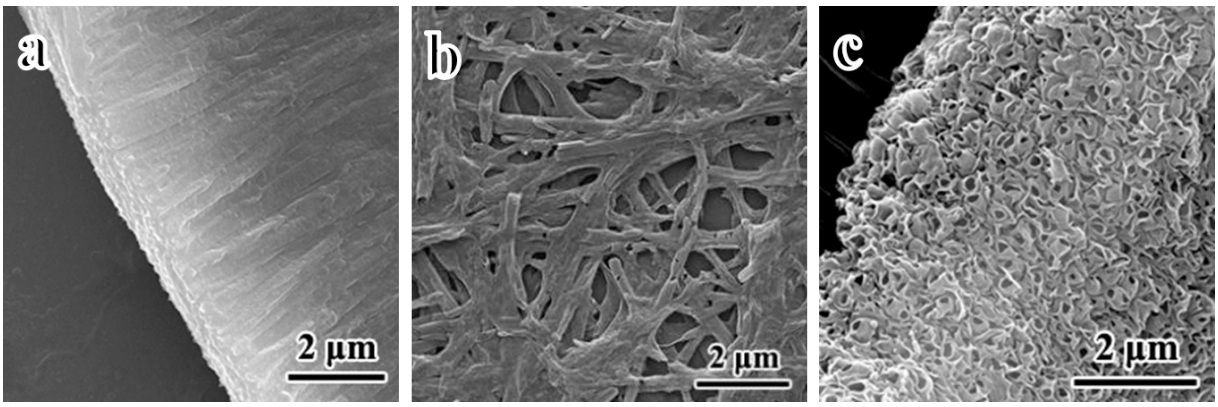

Fig. S6. SEM images of various products: a) S-I-HCSs@CT, b) S-H-HCSs@CT and c) S-CTs.

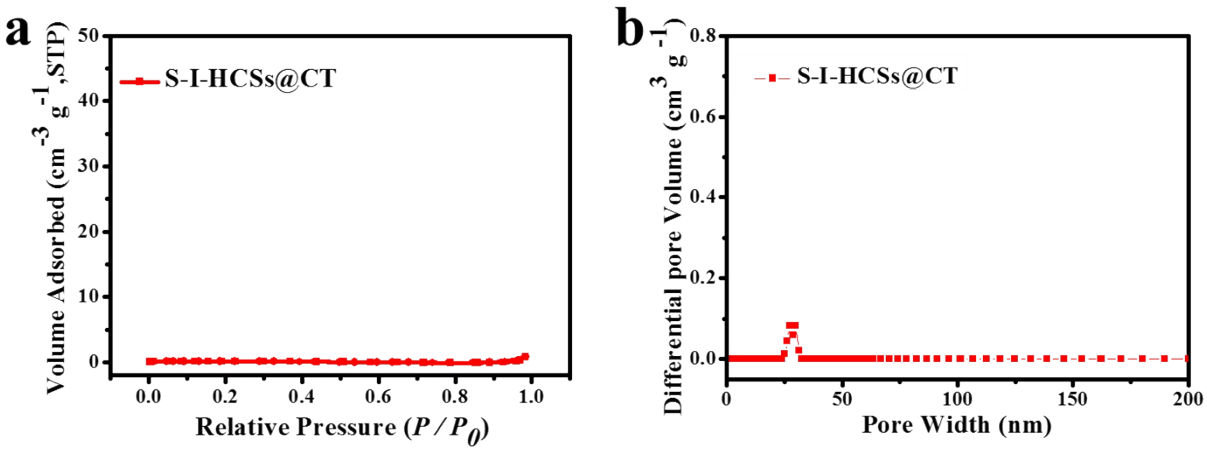

Fig. S7. a) Nitrogen adsorption/desorption isotherms of S-I-HCSs@CT; d) Pore size distribution of S-I-HCSs@CT.

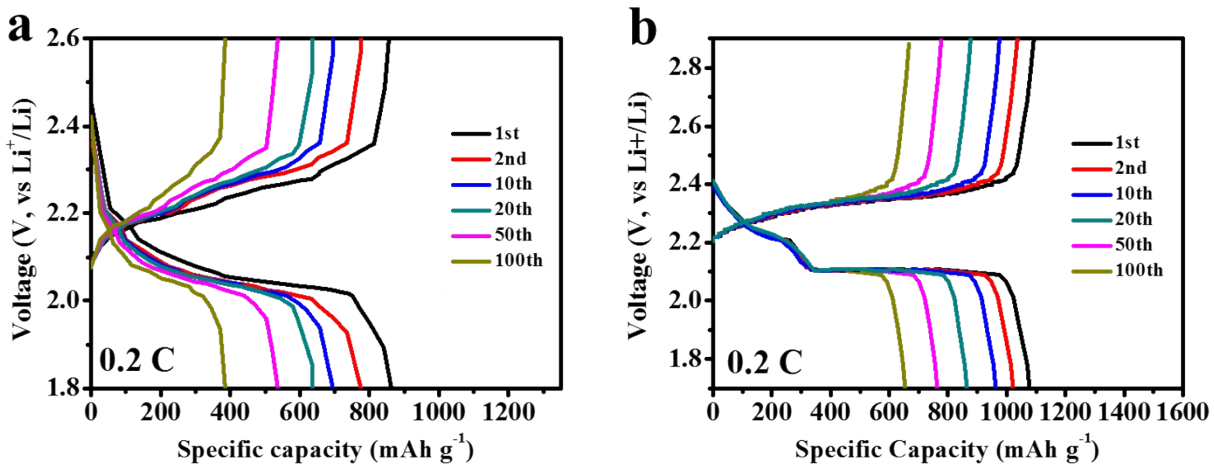

Fig. S8. Discharge/charge voltage profiles of a) S-CTs and b) S-H-HCSs@CT at 0.2C.

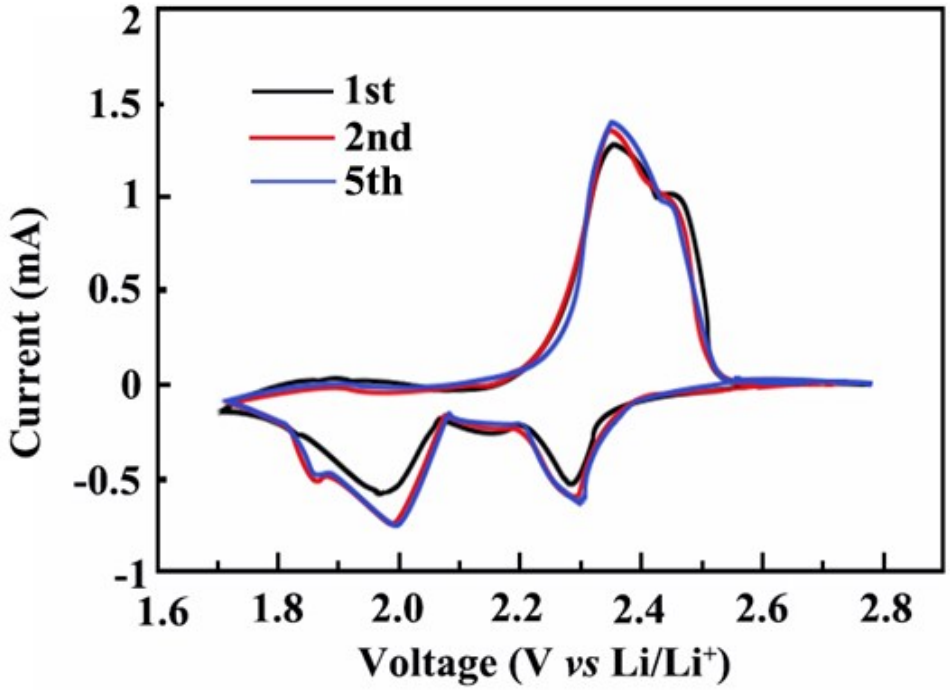

Fig. S9. CV profiles of S-I-HCSs@CT at a scan rate of 0.5 mV s^{-1}.

In the first cathodic scan, there are two well-defined reduction peaks at 2.28 and 2.01 V, corresponding to the multistep reduction mechanism of elemental sulfur. The first peak is the transition from elemental S to long-chain polysulfides (Li_2S_X, $4 < X \leq 8$); the latter is associated with further reduction of the higher polysulfide species (Li_2S_X, $4 < X \leq 8$) to the lower polysulfide species (Li_2S_X, $X \leq 8$). In the anodic scan, there is a shoulder peak at ≈2.39 V and a strong, broader peak at 2.43 V. They are associated with the reverse reactions in the charging stage. In the second anodic scan, the two anodic peaks shift to lower potentials at ≈ 2.36 and ≈ 2.41 V.

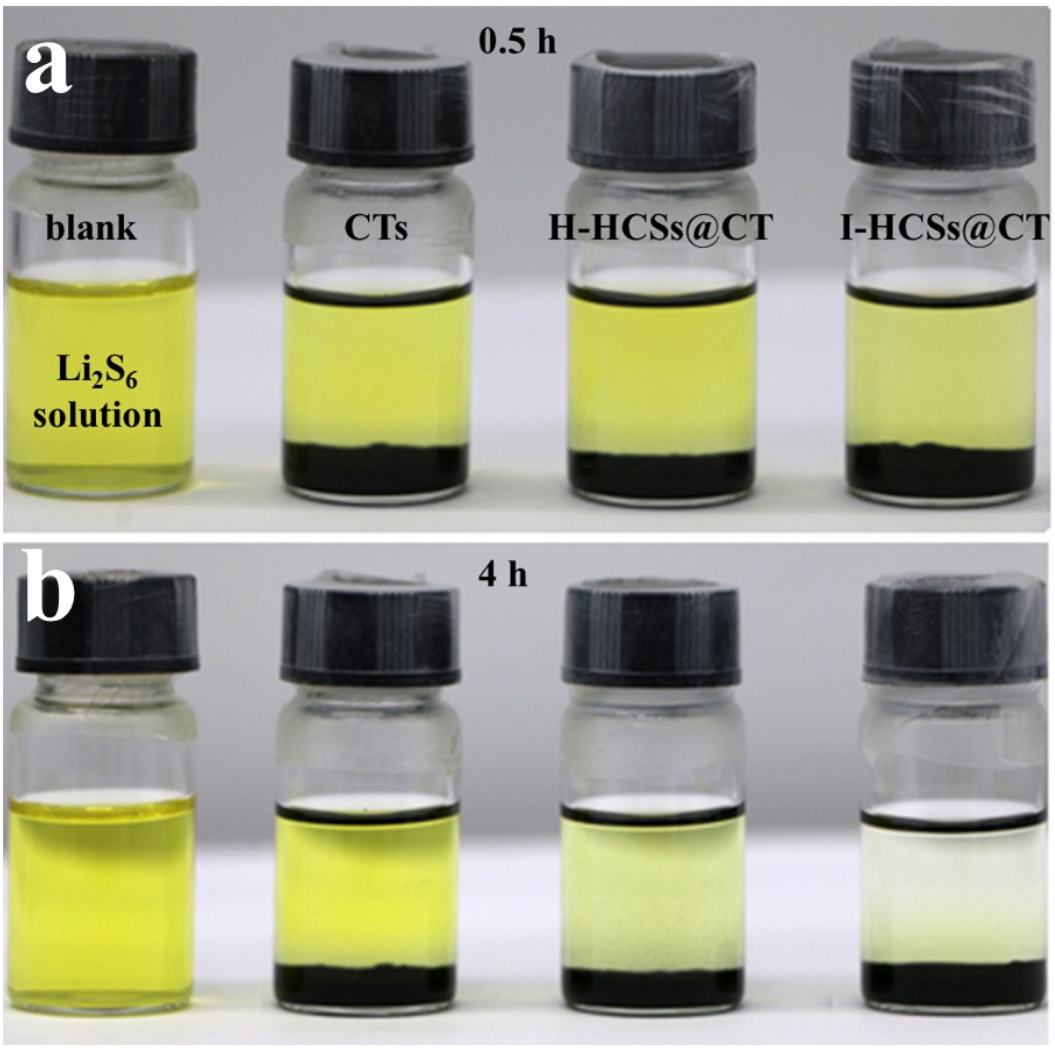

Fig. S10. Digital images of sealed vials with a lithium polysulfides solution (Li_2S_6 dissolved in DOL/DME solvents): a) 0.5 h and b) 4h, after the addition of CTs, H-HCSs@CT and I-HCSs@CT powders.

In Fig. S10a and b, the color of Li_2S_6 solution changed to light yellow after mixing with I-HCSs@CT for 0.5 h, and the solution became almost colorless after 4 h, indicating the strong interaction between I-HCSs@CT and polysulfides.

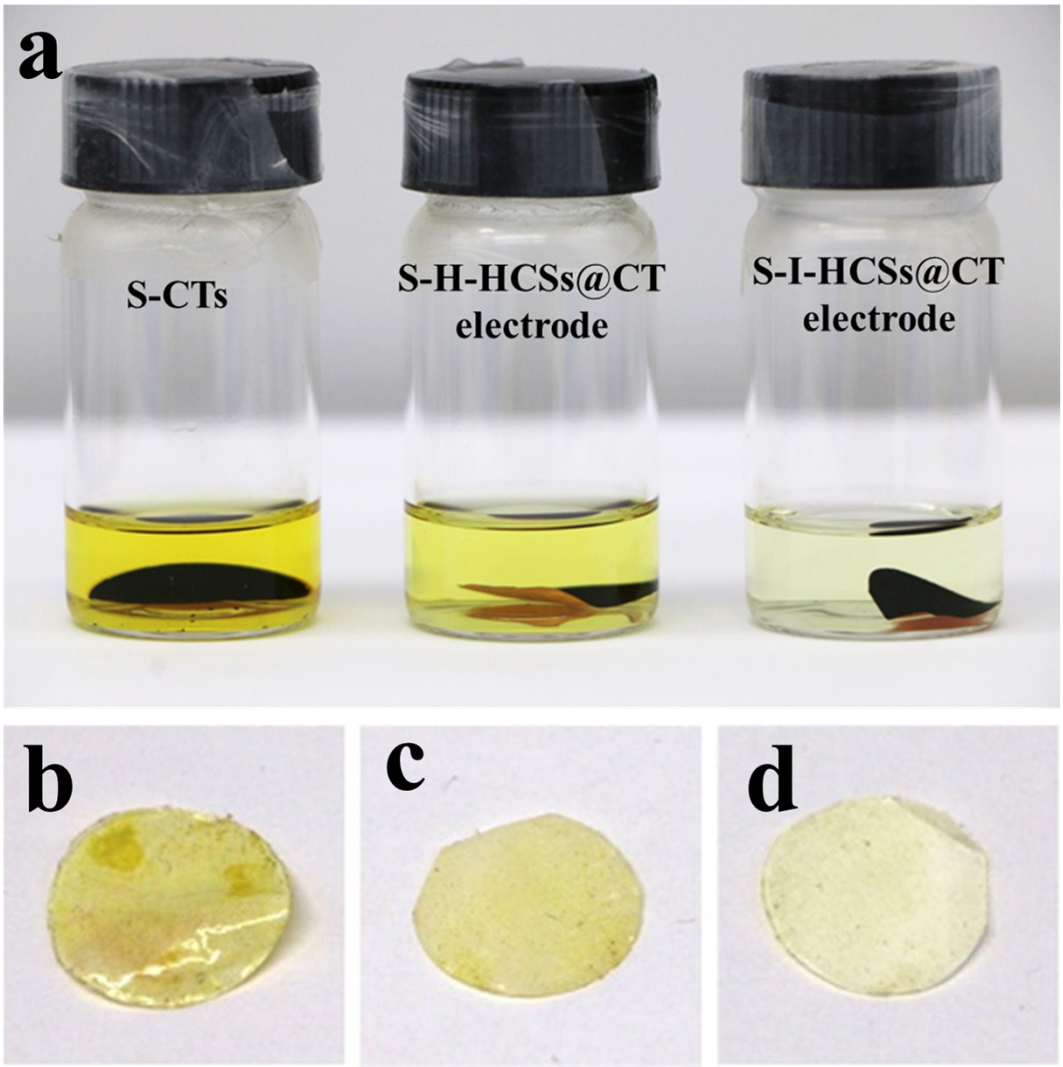

Fig. S11. a) The electrode films of S-CTs, S-H-HCSs@CT and S-I-HCSs@CT cells after 100 cycles, immersing in 5 mL DOL solvent after 1h. Separators from coin cells after 100 cycles of b) S-CTs, c) S-H-HCSs@CT and d) S-I-HCSs@CT.

In Fig. S11, the DOL solution contained the S-H-HCSs@CT and S-CTs electrode and the corresponding separator show much deeper “yellow” color than the S-I-HCSs@CT electrode, indicating the I-HCSs@CT host has much stronger interaction with polysulfides to restrict their dissolution into the organic electrolyte.

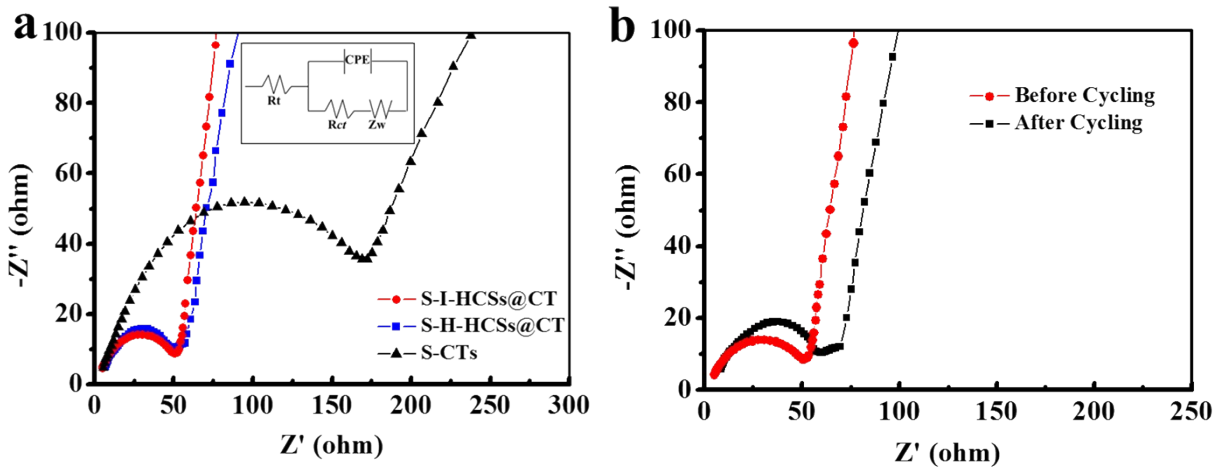

Fig. S12. a) Nyquist plots of S-I-HCSs@CT, S-H-HCSs@CT and S-CTs after the 3rd cycle. b) Nyquist plots of S-I-HCSs@CT before and after 500 cycles at 0.5 C.

Compared with S-CTs, S-I-HCSs@CT and S-H-HCSs@CT has a smaller semicircle, indicating a lower charge transfer resistance (R*ct*) at the electrode interface. The positive effect of HCSs in S-I-HCSs@CT accounts for better high-rate electrochemical performances than S-CTs.

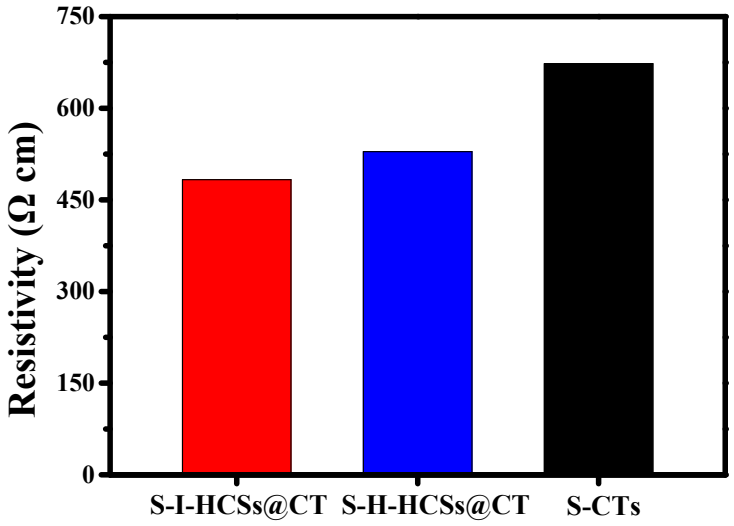

Fig. S13 Electrical resistivity of S-I-HCSs@CT, S-H-HCSs@CT and S-CTs.

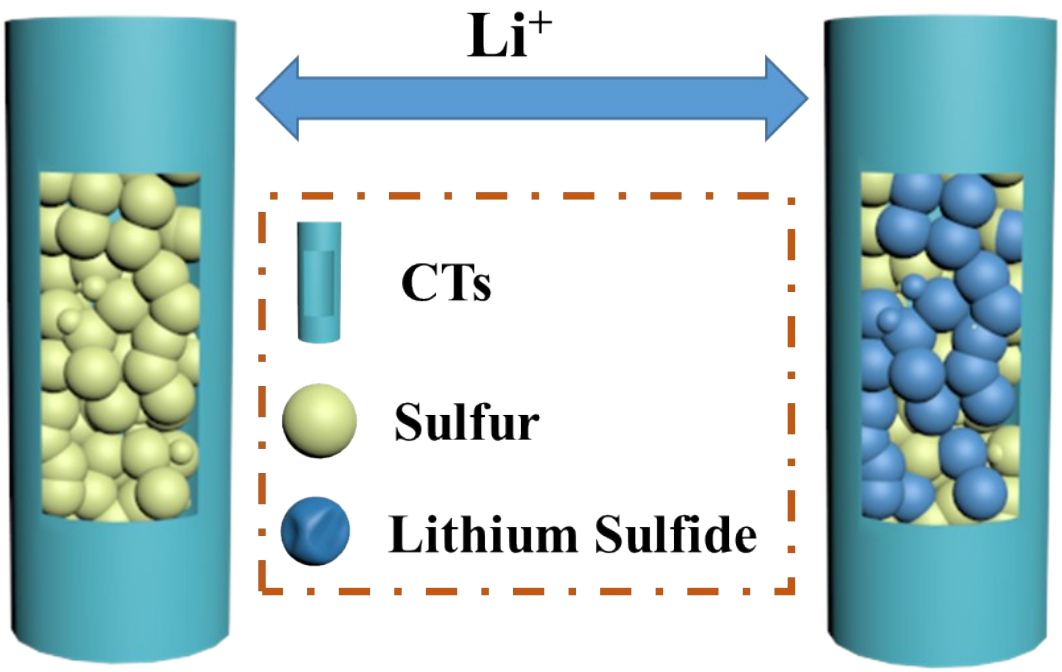

Fig. S14. Schematic diagram of the mechanism for reversible electrochemical reaction of S-CTs.

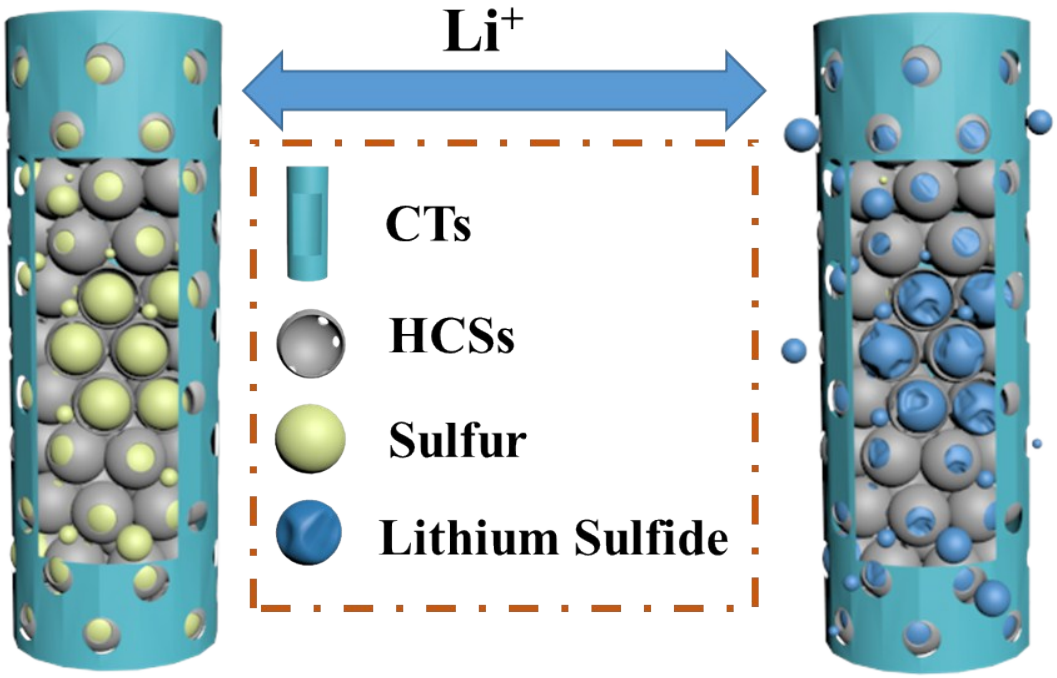

Fig. S15. Schematic diagram of the mechanism for reversible electrochemical reaction of S-H-HCSs@CT.

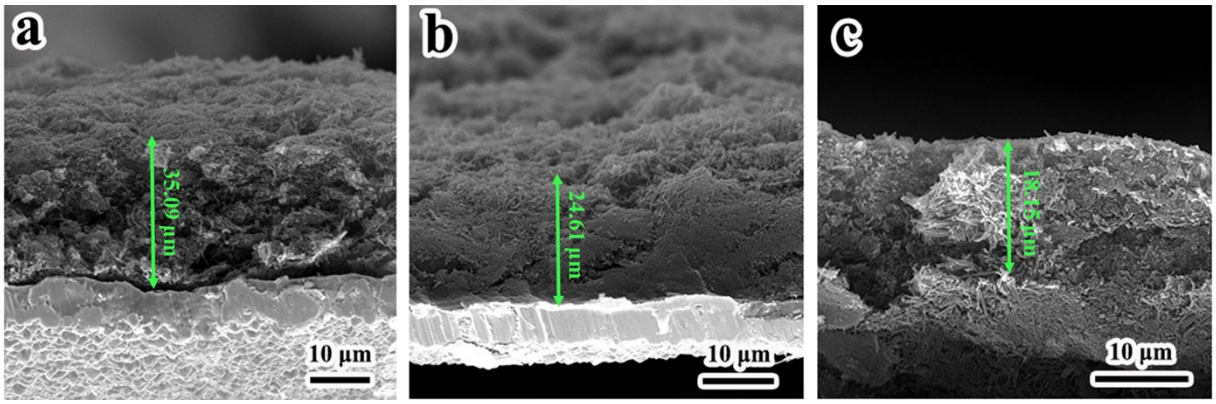

Fig. S16. Cross section SEM images of a) S-CTs, b) S-H-HCS@CT and c) S-I-HCSs@CT after 100 charge/discharge cycles. Compared with the volume change of S-CTs (35.09 μm) and S-H-HCS@CT (24.61 μm)，the S-I-HCSs@CT show smaller volume change (18.15 μm).

Table S1. A comparison of various carbon-based sulfur host materials for lithium sulfur batteries.

Sulfur host materials	Sulfur loading mass	Capacity ($mAh\ g^{-1}$)	Cycling performance ($mAh\ g^{-1}$)	Rention	Ref.
Hollow polymer spheres	/	1179 (0.1 C)	573 (0.5 C, 1000 cycles)	63.7%	1
Hollow carbon spheres	68.1%	1198 (0.2 C)	628 (0.5 C, 200 cycles)	69.8%	2
Disordered carbon nanotubes	59.3%	1543 (0.1 C)	713 (0.1 C, 100 cycles)	46.3%	3
Hollow carbon nanofiber	78.6%	1403 (0.2 C)	730 (0.2 C, 150 cycles)	52.1%	4
N-doped Hollow carbon spheres	/	1126 (0.2 C)	1012 (0.2 C, 100 cycles)	89.9%	5
Double-Shelled Hollow Carbon Spheres	64.1%	1012 (0.1 C)	794 (0.1 C, 100 cycles)	78.5%	6
Holey carbon nanotube	47.4%	1183 (0.2 C)	943 (0.5 C, 200 cycles)	82.0%	7
Graphene oxide	/	1327 (0.02 C)	989 (0.1 C, 55 cycles)	67.1%	8
Reduced graphene oxide	/	1573 (0.1 C)	912 (1 C, 500 cycles)	61.9%	9
MnO_2 filling hollow carbon nanofibers	71.2%	1214 (0.05 C)	736 (0.5 C, 300 cycles)	79.7%	10
Wrapped graphene	70.1%	700 (0.1 C)	600 (0.5 C, 140 cycles)	74.7%	11
Porous hollow carbon	/	1186	991	71.4%	12

		(0.1 C)	(0.5 C, 100 cycles)		
Ordered Mesoporous Carbon Nanoparticles	70.0%	1163 (1C)	845 (1 C, 100 cycles)	72.6%	13
Multichannel Carbon Nanofiber	80.0%	1385 (0.2 C)	1013 (0.2 C, 300 cycles)	72.7%	14
Tube-in-tube carbon nanotube	71.2%	1273 (0.5 A g^{-1})	647 (2 A g^{-1}, 200 cycles)	58.1%	15
Sphere-in-tube carbon nanostructures	72.1%	1426 (0.1 C)	746 (0.5 C, 500 cycles)	80.4%	This work

References

[1] W.Y. Li, G.Y. Zheng, Y. Yang, Z. W. Seh, N. Liu, Y. Cui, *Proc. Natl. Acad. Sci. U.S.A.*, 2013, **110**, 7148-7153.

[2] W.D. Zhou, Y.C. Yu, H. Chen, F.J. DiSalvo, H.D. Abruña, *J. Am. Chem. Soc.*, 2013, **135**, 16736-16743

[3] J.C. Guo, Y.H. Xu, C.S. Wang, *Nano Lett.*, 2011, **11**, 4288-4294

[4] G.Y. Zheng, Y. Yang, J.J. Cha, S.S. Hong, Y. Cui, *Nano Lett.*, 2011, **11**, 4462-4467

[5] W.D. Zhou, C.M. Wang, Q.L. Zhang, H.D. Abruña, Y. He, J.W. Wang, S.X. Mao, X.C. Xiao, *Adv. Energy Mater.*, 2015, **5**, 1401752.

[6] C.F. Zhang, H.B. Wu, C.Z. Yuan, Z.P. Guo, X.W.D. Lou, *Angew. Chem. Int. Ed.*, 2012, **124**, 9730-9733

[7] Y. Zhou, C.G. Zhou, Q.Y. Li, C.J. Yan, B. Han, K.S. Xia, Q. Gao, J. Wu, *Adv. Mater.*, 2015, **27**, 3774-3781

[8] L.W. Ji, M.M. Rao, H.M. Zheng, L. Zhang, Y.C. Li, W.H. Duan, J.H. Guo, E.J. Carins, Y. G. Zhang, *J. Am. Chem. Soc.*, 2011, **133**, 18522-18525

[9] P.T. Xiao, F.X. Bu, G.H. Yang, Y. Zhang, Y.X. Xu, *Adv. Mater.*, 2017, **29**, 1703324.

[10] Z. Li, J.T. Zhang, X.W.D. Lou, *Angew. Chem. Int. Ed.*, 2015, **54**, 12886-12890

[11] H.L. Wang, Y. Yang, Y.G. Liang, J.T. Robinson, Y.G. Li, A. Jackson, Y. Cui, H.J. Dai, *Nano Lett.*, 2011, **11**, 2644-2647

[12] N. Jayaprakash, J. Shen, S.S. Moganty, A. Corona, L.A. Archer, *Angew. Chem. Int. Ed.*, 2011, **123**, 6026-6030

[13] H. Ye, Y.X. Yin, S. Xin, Y.G. Guo, *J. Mater. Chem. A*, 2013, **1**, 6602-6608

[14] J.S. Lee, W. Kim, J. Jang, A. Manthiram, *Adv. Energy Mater.*, 2017, **7**, 1601543.

[15] Y. Zhao, W.L. Wu, J.X. Li, Z.C. Xu, L.H. Guan, *Adv. Mat.*, 2014, **26**, 5113-5118.